liquids

MDPI

Article

Coupled Momentum, Heat and Mass Transport in Steady Two-Dimensional Flow of a Casson Ternary Hybrid Nanofluid over a Stretching Surface Under a Transverse Magnetic Field with Velocity and Thermal Slip

Jagadish V. Tawade [1,2,*], C. Balarama Krishna [2], Mahadev M. Biradar [3], Ranjit Vasant Rajale [4], Avinash Raut [5] and Machindranath Diwate [5]

1 Department of Mathematics, Vishwakarma University, Pune 411048, India
2 Department of Mathematics, SR University, Warangal 506371, India
3 Department of Mathematics, Basaveshwar Engineering College, Bagalkote 587102, India
4 Research Scholar, Department of Mechanical Engineering, Shri Jagdishprasad Jhabarmal Tibrewala University (JJTU), Jhunjhunu 333001, India
5 Department of Mathematics, Vishwakarma Institute of Technology, Pune 411048, India; avinash.raut@vit.edu (A.R.)
* Correspondence: jagadish.tawade@vupune.ac.in

Abstract

This study investigates the steady, two-dimensional incompressible boundary layer flow, with coupled heat and mass transfer, of a Casson ternary hybrid nanofluid (Al_2O_3–Cu–TiO_2/water) over a linearly stretching surface subject to a transverse magnetic field, thermal radiation, internal heat generation/absorption, a first-order chemical reaction, and velocity and thermal slip. The Casson model represents the yield-stress and shear-thinning rheology of the base fluid, and the effective properties of the ternary mixture are evaluated from established mixture and Maxwell-type correlations. Similarity transformations reduce the governing partial differential equations to a system of nonlinear ordinary differential equations, which is solved numerically with the NDSolve routine of Mathematica and, for validation, analytically by a regular perturbation expansion in the small parameter $\epsilon = 1/\beta$ (large Casson parameter). The effects of the Casson parameter, magnetic parameter, radiation parameter, heat source parameter, Schmidt number and chemical reaction parameter on the velocity, temperature and concentration profiles, and on the skin friction coefficient, Nusselt number and Sherwood number, are discussed. The numerical and perturbation solutions agree to within 0.6% at $\beta = 1.5$. Increasing the Casson parameter thins the momentum boundary layer and reduces the magnitude of the skin friction coefficient by 31.7% (from $\beta = 0.5$ to 2.5), whereas it thickens the thermal and concentration boundary layers. The magnetic field retards the flow, thermal radiation and heat generation raise the temperature, and larger Schmidt numbers and reaction rates thin the concentration boundary layer. The results are useful for the design of thermal and materials-processing systems that employ multi-component nanofluids with complex rheology.

Keywords: ternary hybrid nanofluid; Casson fluid; perturbation method; numerical solution; heat and mass transfer; stretched surface; boundary layer flow; magnetohydrodynamics; velocity and thermal slip

Check for updates

Academic Editor: Enrico Bodo

Received: 19 October 2026
Revised: 9 November 2026
Accepted: 12 November 2026
Published: 26 November 2026

Copyright: © 2026 by the authors. Licensee MDPI, Basel, Switzerland. This article is an open access article distributed under the terms and conditions of the Creative Commons Attribution (CC BY) license.

1. Introduction

1.1. Motivation and Background

A major challenge facing the industry today is the ability to develop thermal transport systems that improve heat and mass transfer properties. In many applications within engineering and industry, including Biomedical Systems [1], Solar Energy Collection [2], Advanced Manufacturing Processes [3], and Micro Electronics Cooling [4], conventional heat transfer fluids such as water, Ethylene Glycol, and Engine Oil are limited in thermal conductivity to levels below those of current technologies.

In 1995, Choi and Eastman [5] introduced an innovative concept—nanofluids, which are categorized as engineered colloidal suspensions consisting of nanometer-sized particles suspended in base fluids. Compared to base fluids used with conventional heat exchanger systems, the presence of these nanoparticles produces a significant thermal enhancement.

Nanofluid technology has evolved from the basic Mono-Nanofluids to sophisticated hybrid nanofluids (two types of nanoparticles). Hybrid systems utilize the Synergistic Effects of various nanomaterials to produce better thermal properties, improve stability, and provide Multifunctional Properties that are not achievable in single-particle systems [6].

The recent advancements of ternary hybrid nanofluids (THNFs; Three Types of Nanoparticles) mark the leading edge of research in nanofluids [7,8]. In addition, THNFs have shown superior thermal performance compared to Mono-Nanofluids and hybrid nanofluids, as confirmed by [9,10], with additional studies relating to THNF Synthesis [11], THNF Stability [12], and THNF Thermophysical Properties [13].

It is also important to note that many fluids of industrial and physiological significance have characteristics of non-Newtonian fluids, where their viscosity will vary based on the amount of shear stress applied [14].

Developed for pigment-oil suspensions by Casson [15], the Casson fluid model has been most useful in modeling a variety of complex fluids including blood, food materials, and some nanomaterials [16,17]. Such behavior is of paramount importance for the realistic mathematical modeling of various industrial processes, since it correctly accounts for both the yield-stress and shear-thinning properties exhibited by many real fluids.

1.2. Literature Review and Research Gap

A simple configuration in fluid dynamics, the flow over a stretched surface has numerous applications for material synthesis such as wire drawing, glass blowing, polymer and metal production [18,19]. In industrial applications, notably, the flow over a stretching surface has been used to predict heat and mass transfer rates on the final product [20]. The boundary slip observed by [21,22] can influence heat transfer characteristics and flow dynamics. The velocity and thermal slip [23,24] parameters are very important to accurately predict the behaviors in micro-electro-mechanical systems as well as nanochannels, based on investigations on various nanofluids.

The integration of hybrid nanofluid technology and non-Newtonian fluid models has been an ongoing research trend. Numerous characteristics of Williamson hybrid nanofluids [25] and Casson hybrid nanofluids [26] over various geometries have been studied. Gowda et al. [27] for Casson nanofluids and Megahed [28] for improving heat transfer mechanisms have both looked at the effect of slip conditions on such flows. In addition, there has been a lot of interest in the stability of dual solutions in slip flow regimes [29].

Recent studies have extended these models to increasingly complex transport settings. Arif et al. [30] simulated three-dimensional MHD flow of an Fe_3O_4–Cu/water hybrid nanofluid in a rotating Darcy–Forchheimer porous medium with thermal radiation, internal heat generation, velocity slip, and chemical reaction, and solved the boundary-value problem with a hybrid artificial-intelligence approach based on Morlet wavelet neural networks

and particle swarm optimization. Ullah et al. [31] analyzed three-dimensional MHD flow of a Prandtl ternary (Cu–Fe_3O_4–$CoFe_2O_4$/water) nanofluid with porosity, Darcy–Forchheimer drag, radiation, and activation energy over a stretching surface with convective boundary conditions. Aslam et al. [32] combined bvp4c solutions with a Levenberg–Marquardt artificial neural network to study MHD Williamson CuO–Cu/blood hybrid nanofluid flow with Cattaneo–Christov heat and mass flux over a stretching cylinder, and Ali et al. [33] obtained numerical (bvp4c) and analytical (homotopy analysis) solutions for Darcy–Forchheimer flow of a Williamson nanofluid with Cattaneo–Christov heat flux and thermal stratification over a Riga plate. These works show the growing interest in multi-component nanofluids with non-Newtonian rheology and magnetic control, and in verifying numerical solutions by independent analytical or data-driven techniques.

Studies dealing specifically with Casson ternary hybrid nanofluids are still relatively few. Saleem et al. [34] considered an Ag–Cu–TiO_2/oil Casson ternary nanofluid over a vertically stretching sheet with electromagnetohydrodynamic forcing, Thomson–Troian velocity slip, thermal slip, radiation and Joule heating, solved with the RKF-45 method; Kezzar et al. [35] studied MHD flow of a blood-based Casson ternary hybrid nanofluid in converging/diverging channels with velocity slip by the Duan–Rach approach and the RKF-45 method; and Patnaik et al. [36] investigated Bödewadt slip flow of an Al_2O_3–CNT–graphene/water Casson ternary hybrid nanofluid over a stretching rotating disk with second-order slip. For the same Cu–Al_2O_3–TiO_2/water combination as considered here, Nath and Deka [37] analyzed MHD flow past a vertically stretching cylinder in a porous medium with thermal stratification and reported higher heat transfer rates for the ternary mixture than for the hybrid and Mono-Nanofluids, while Cao et al. [38] examined the dynamics of water-based ternary hybrid nanofluids at different levels of partial slip. In contrast to these studies, the present model (i) couples momentum, heat, and mass transfer with a first-order chemical reaction for a Casson Al_2O_3–Cu–TiO_2/water ternary hybrid nanofluid over a linearly stretching sheet, (ii) imposes velocity and thermal slip simultaneously, and (iii) verifies the numerical solution with a regular perturbation expansion in the inverse Casson parameter rather than relying on a single numerical scheme.

However, there is still much to learn about integrating the Casson fluid model with ternary hybrid nanofluid systems, particularly in terms of flow over stretching surfaces with simultaneous heat and mass transfer considerations, as well as the effects of velocity and thermal slip [39,40]. Given the potential applications of such complex fluids in materials processing, biomedical engineering, and sophisticated thermal management systems, where slip events may be common, the research gap is significant.

1.3. Novelty and Contributions of the Present Study

The present study differs from, and advances, the existing literature in three specific ways. (1) Model: to the best of our knowledge, it is the first study to combine Casson rheology, an Al_2O_3–Cu–TiO_2/water ternary hybrid mixture, simultaneous velocity and thermal slip, a transverse magnetic field, thermal radiation, internal heat generation/absorption, and a first-order chemical reaction in a single coupled momentum–heat–mass transfer model over a stretching surface. (2) Method: the numerical NDSolve solution, in which the slip conditions are imposed as Robin-type constraints, is verified independently by a second-order regular perturbation expansion in $\epsilon = 1/\beta$, and the momentum problem is shown to admit a closed-form solution that gives the first- and second-order Casson corrections explicitly. (3) Physical insight: the closed-form solution shows that the Casson parameter, the magnetic parameter, and the nanoparticle loading act through a single decay rate, so that the Casson effect on the wall shear stress follows the universal factor $\sqrt{1 + 1/\beta}$, independent of the magnetic parameter and of the nanoparticle volume

fractions, and the one-way coupling of the momentum equation to the thermal and solutal fields explains why the radiation, heat source, Schmidt, and reaction parameters leave the velocity field unchanged.

1.4. Objectives and Organization of the Paper

Inspired by these characteristics, the current study investigates the mass and heat transfer properties of a ternary hybrid nanofluid (Al_2O_3-Cu-TiO_2) based on Casson fluid across a stretched surface, taking into account velocity and thermal slip effects. The research's specific goals are to:

1. develop a comprehensive mathematical model that includes Casson fluid rheology, ternary hybrid nanofluid thermophysical properties, and slip boundary conditions;
2. obtain numerical solutions using Mathematica;
3. derive analytical solutions for validation using perturbation methods; and
4. investigate how different physical parameters, including slip parameters, affect flow, heat, and mass transfer characteristics.

The purpose of this research is to provide valuable insights into the design and optimization of advanced thermal systems that employ complicated nanofluids with specialized properties.

The remainder of the paper is organized as follows. Section 2 presents the mathematical formulation, the slip boundary conditions, the similarity transformation, and the property models of the ternary hybrid nanofluid. Section 3 develops the perturbation solution, including closed-form zeroth-, first-, and second-order momentum solutions. Section 4 describes the numerical method. Section 5 presents and interprets the velocity, temperature, and concentration profiles. Section 6 discusses the skin friction, Nusselt and Sherwood numbers, the validation of the perturbation solution, and the comparison with benchmark solutions. Section 7 summarizes the contributions, practical implications, and limitations of the study.

2. Mathematical Formulation

The schematic representation of the physical configuration for Casson ternary hybrid nanofluid flow over a stretching surface with velocity and thermal slip effects under the influence of a magnetic field is shown in Figure 1. A stretching surface has a linearly varying velocity; therefore, the velocity, temperature, and nanoparticle concentration boundary-layer profiles can be represented by $f'(\eta)$, $\theta(\eta)$, *and* $\phi(\eta)$, respectively.

2.1. Governing Equations

The flow is considered to be steady, two-dimensional, and incompressible. The governing equations for mass, momentum, energy, and concentration conservation are given by:

2.1.1. Continuity Equation

$$\frac{\partial u}{\partial x} + \frac{\partial v}{\partial y} = 0 \tag{1}$$

2.1.2. Momentum Equation

$$u\frac{\partial u}{\partial x} + v\frac{\partial u}{\partial y} = \frac{\mu_{thnf}}{\rho_{thnf}}\left(1 + \frac{1}{\beta}\right)\frac{\partial^2 u}{\partial y^2} - \frac{\sigma_{thnf}B_0^2}{\rho_{thnf}}u \tag{2}$$

where β is the Casson fluid parameter.

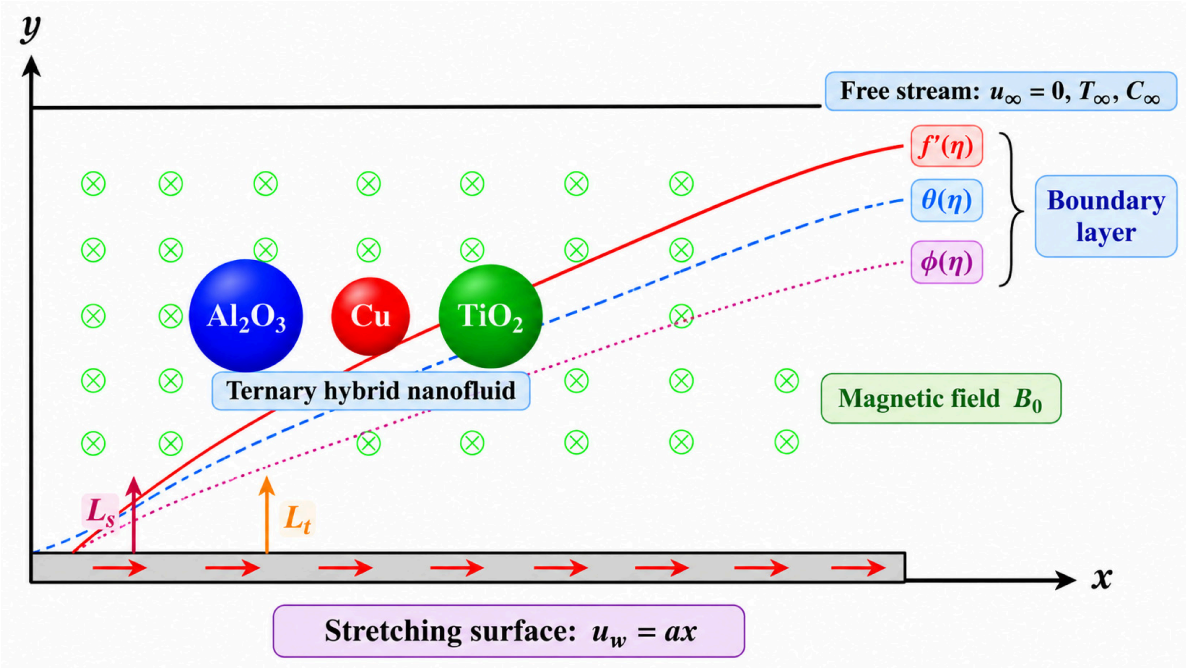

Figure 1. Physical configuration of Casson ternary hybrid nanofluid flow over a stretching surface with velocity and thermal slip effects.

2.1.3. Energy Equation

$$u\frac{\partial T}{\partial x} + v\frac{\partial T}{\partial y} = \frac{k_{thnf}}{(\rho C_p)_{thnf}}\frac{\partial^2 T}{\partial y^2} - \frac{1}{(\rho C_p)_{thnf}}\frac{\partial q_r}{\partial y} + \frac{Q_0}{(\rho C_p)_{thnf}}(T - T_\infty) \tag{3}$$

where $q_r = -\frac{4\sigma^*}{3k^*}\frac{\partial T^4}{\partial y}$ is the radiative heat flux. Here σ^* is the Stefan–Boltzmann constant and k^* is the mean absorption coefficient; with the Rosseland approximation and the expansion $T^4 \approx 4T_\infty^3 T - 3T_\infty^4$, the radiative term becomes linear in T.

2.1.4. Concentration Equation

$$u\frac{\partial C}{\partial x} + v\frac{\partial C}{\partial y} = D_{thnf}\frac{\partial^2 C}{\partial y^2} - K_r(C - C_\infty) \tag{4}$$

2.2. Slip Boundary Conditions

To account for micro-scale effects and certain fluid–surface interactions, the classical no-slip condition is modified. The dimensional boundary conditions at the stretching sheet are given by:

$$u = U_w(x) + U_{slip} = ax + L_s\frac{\partial u}{\partial y}, \quad v = 0, \quad T = T_w + T_{slip} = T_w + L_t\frac{\partial T}{\partial y},$$

$$C = C_w \quad at \quad y = 0 \tag{5}$$

$$u \to 0, \quad T \to T_\infty, \quad C \to C_\infty \quad as \quad y \to \infty \tag{6}$$

where L_s is the velocity slip length and L_t is the thermal slip length. Because they relate the value of the velocity (temperature) at the wall to its wall-normal derivative, the slip conditions in Equation (5) are mixed (Robin-type) boundary conditions; for $L_s = L_t = 0$ they reduce to the classical no-slip (Dirichlet) conditions.

2.3. Similarity Transformations

To convert the partial differential equations into ordinary differential equations, we introduce the following similarity variables:

$$\eta = y\sqrt{\frac{a}{\nu_f}}, \tag{7}$$

where $a > 0$ (s^{-1}) is the stretching-rate constant of the sheet ($U_w = ax$) and $\nu_f = \mu_f/\rho_f$ is the kinematic viscosity of the base fluid

$$\psi = x\sqrt{a\nu_f}f(\eta), \tag{8}$$

$$\theta(\eta) = \frac{T - T_\infty}{T_w - T_\infty}, \tag{9}$$

$$\phi(\eta) = \frac{C - C_\infty}{C_w - C_\infty} \tag{10}$$

where the stream function ψ satisfies:

$$u = \frac{\partial \psi}{\partial y}, \quad v = -\frac{\partial \psi}{\partial x} \tag{11}$$

2.4. Non-Dimensional Equations

Applying the similarity transformations, we obtain the following system of ordinary differential equations:

$$\left(1 + \frac{1}{\beta}\right)\frac{\mu_{thnf}/\mu_f}{\rho_{thnf}/\rho_f}f''' + ff'' - (f')^2 - \frac{\sigma_{thnf}/\sigma_f}{\rho_{thnf}/\rho_f}Mf' = 0 \tag{12}$$

$$\frac{1}{Pr}\frac{k_{thnf}/k_f}{\left(\rho C_p\right)_{thnf}/\left(\rho C_p\right)_f}\left(1 + \frac{4}{3}R_d\right)\theta'' + f\theta' + \frac{Q}{\left(\rho C_p\right)_{thnf}/\left(\rho C_p\right)_f}\theta = 0 \tag{13}$$

$$\frac{1}{Sc}\frac{D_{thnf}}{D_f}\phi'' + f\phi' - K\phi = 0 \tag{14}$$

2.5. Boundary Conditions (Non-Dimensional)

Applying the similarity transformations to Equations (5) and (6), the non-dimensional boundary conditions become:

$$f(0) = 0, \quad f'(0) = 1 + \lambda_s f''(0), \quad \theta(0) = 1 + \lambda_t \theta'(0), \quad \phi(0) = 1 \tag{15}$$

$$f'(\eta) \to 0, \quad \theta(\eta) \to 0, \quad \phi(\eta) \to 0 \quad as \quad \eta \to \infty \tag{16}$$

where $\lambda_s = L_s\sqrt{a/\nu_f}$ is the dimensionless velocity slip parameter and $\lambda_t = L_t\sqrt{a/\nu_f}$ is the dimensionless thermal slip parameter.

The velocity condition in Equation (5) is the Navier slip condition: the fluid adjacent to the sheet does not move with the sheet velocity U_w but lags behind it by an amount proportional to the local shear rate, the proportionality constant being the slip length L_s. Such slip occurs in micro- and nano-scale flows, over hydrophobic or coated surfaces and in particle-laden suspensions, in which a particle-depleted layer may form at the wall. The thermal condition is the corresponding temperature-jump condition, according to which the fluid temperature at the wall differs from T_w by an amount proportional to the wall-normal temperature gradient, with thermal slip length L_t. The dimensionless parameters λ_s and λ_t measure these slip lengths relative to the viscous length scale $\sqrt{\nu_f/a}$. For $\lambda_s = \lambda_t = 0$, the no-slip and prescribed-temperature conditions are recovered. Increasing λ_s reduces the momentum transmitted from the sheet to the fluid (for the zeroth-order solution of Section 3.7, $f_0'(0) = 1/(1 + \lambda_s\gamma)$), and increasing λ_t lowers the fluid temperature at the wall ($\theta_0(0) = 1/(1 + \lambda_t\delta)$) and hence the wall heat flux.

2.6. Non-Dimensional Parameters

The non-dimensional parameters appearing in the equations are defined as:

- $M = \frac{\sigma_f B_0^2}{a\rho_f}$ (Magnetic parameter). An increase in M strengthens the Lorentz drag that opposes the flow, which decelerates the fluid, thins the momentum boundary layer, and increases the wall velocity gradient.
- $\mathrm{Pr} = \frac{\nu_f}{\alpha_f}$ (Prandtl number). A larger Pr means that heat diffuses more slowly than momentum, which produces a thinner thermal boundary layer and a higher wall heat transfer rate.
- $R_d = \frac{4\sigma^* T_\infty^3}{k^* k_f}$ (Radiation parameter). Increasing Rd enhances radiative heat transport, which acts as an additional effective conductivity (factor $1 + 4\mathrm{Rd}/3$) and therefore raises the temperature and thickens the thermal boundary layer.
- $Q = \frac{Q_0}{a(\rho C_p)_f}$ (Heat source/sink parameter). Increasing $Q > 0$ (heat generation) supplies internal heat and raises the temperature in the boundary layer, whereas $Q < 0$ (heat absorption) has the opposite effect.
- $Sc = \frac{\nu_f}{D_f}$ (Schmidt number). An increase in Sc signifies weaker mass diffusivity relative to momentum diffusivity, which thins the concentration boundary layer and increases the wall mass transfer rate.
- $K = \frac{K_r}{a}$ (Chemical reaction parameter). Increasing K (destructive reaction) consumes the diffusing species more rapidly, which reduces the concentration and thins the concentration boundary layer.
- $\beta = \mu_B\sqrt{2\pi_c}/p_y$ (Casson fluid parameter; μ_B plastic viscosity, π_c critical value of the product of the deformation-rate components, p_y yield stress). An increase in β weakens the yield stress and reduces the effective viscosity factor $(1 + 1/\beta)$, so that the fluid approaches Newtonian behavior ($\beta \to \infty$); in the present problem, this thins the momentum boundary layer and reduces the wall shear stress (Table 1).

Table 1. Reduced skin friction coefficient $C_f^* = (1 + 1/\beta)f''(0)$, reduced Nusselt number $Nu^* = -\theta'(0)$ and reduced Sherwood number $Sh^* = -\phi'(0)$ for different values of the Casson parameter β ($M = 1.0$, $\phi_1 = \phi_2 = \phi_3 = 0.01$, $R_d = 0.3$, $Q = 0.1$, $Sc = 0.6$, $K = 0.2$, $\lambda_s = \lambda_t = 0$).

$\boldsymbol{\beta}$	$\boldsymbol{C_f^*}$	$\boldsymbol{Nu^*}$	$\boldsymbol{Sh^*}$
0.5	−1.883	0.969	0.592
1.0	−1.537	0.961	0.572
1.5	−1.403	0.956	0.562
2.0	−1.331	0.954	0.556
2.5	−1.286	0.952	0.553

2.7. Ternary Hybrid Nanofluid Properties

The thermophysical properties of the ternary hybrid nanofluid are calculated as follows:

2.7.1. Density

$$\rho_{thnf} = (1 - \phi_1 - \phi_2 - \phi_3)\rho_f + \phi_1\rho_{s1} + \phi_2\rho_{s2} + \phi_3\rho_{s3} \tag{17}$$

2.7.2. Heat Capacity

$$\left(\rho C_p\right)_{thnf} = (1 - \phi_1 - \phi_2 - \phi_3)\left(\rho C_p\right)_f + \phi_1\left(\rho C_p\right)_{s1} + \phi_2\left(\rho C_p\right)_{s2} + \phi_3\left(\rho C_p\right)_{s3} \tag{18}$$

2.7.3. Dynamic Viscosity

$$\mu_{thnf} = \frac{\mu_f}{(1-\phi_1-\phi_2-\phi_3)^{2.5}} \tag{19}$$

2.7.4. Thermal Conductivity

$$\frac{k_{thnf}}{k_f} = \frac{k_{s3} + 2k_{hnf} - 2\phi_3\left(k_{hnf} - k_{s3}\right)}{k_{s3} + 2k_{hnf} + \phi_3\left(k_{hnf} - k_{s3}\right)} \tag{20}$$

$$\frac{k_{hnf}}{k_f} = \frac{k_{s2} + 2k_{nf} - 2\phi_2\left(k_{nf} - k_{s2}\right)}{k_{s2} + 2k_{nf} + \phi_2\left(k_{nf} - k_{s2}\right)} \tag{21}$$

$$\frac{k_{nf}}{k_f} = \frac{k_{s1} + 2k_f - 2\phi_1\left(k_f - k_{s1}\right)}{k_{s1} + 2k_f + \phi_1\left(k_f - k_{s1}\right)} \tag{22}$$

2.7.5. Electrical Conductivity

$$\frac{\sigma_{thnf}}{\sigma_f} = \frac{\sigma_{s3} + 2\sigma_{hnf} - 2\phi_3\left(\sigma_{hnf} - \sigma_{s3}\right)}{\sigma_{s3} + 2\sigma_{hnf} + \phi_3\left(\sigma_{hnf} - \sigma_{s3}\right)} \tag{23}$$

$$\frac{\sigma_{hnf}}{\sigma_f} = \frac{\sigma_{s2} + 2\sigma_{nf} - 2\phi_2\left(\sigma_{nf} - \sigma_{s2}\right)}{\sigma_{s2} + 2\sigma_{nf} + \phi_2\left(\sigma_{nf} - \sigma_{s2}\right)} \tag{24}$$

$$\frac{\sigma_{nf}}{\sigma_f} = \frac{\sigma_{s1} + 2\sigma_f - 2\phi_1\left(\sigma_f - \sigma_{s1}\right)}{\sigma_{s1} + 2\sigma_f + \phi_1\left(\sigma_f - \sigma_{s1}\right)} \tag{25}$$

2.7.6. Mass Diffusivity

$$D_{thnf} = \frac{D_f}{(1-\phi_1-\phi_2-\phi_3)^{2.5}} \tag{26}$$

where ϕ_1, ϕ_2, and ϕ_3 represent the volume fractions of Al_2O_3, Cu, and TiO_2 nanoparticles, respectively. The subscripts $s1$, $s2$ and $s3$ denote the Al_2O_3, Cu and TiO_2 particles, and nf, hnf and $thnf$ denote, respectively, the Al_2O_3/water nanofluid, the Al_2O_3–Cu/water hybrid nanofluid and the Al_2O_3–Cu–TiO_2/water ternary hybrid nanofluid; the Maxwell-type relations (20)–(25) are thus applied successively, each time treating the previous mixture as the host fluid. The thermophysical properties of the base fluid and the nanoparticles used in the computations, and the volume fractions $\phi_1 = \phi_2 = \phi_3 = 0.01$ (total loading 3%), are listed in Table A1 (Appendix A) [41]. Equations (17)–(26) are classical correlations for dilute suspensions of spherical particles and are therefore applicable at such low volume fractions.

2.8. Physical Quantities of Interest

The skin friction coefficient C_f, Nusselt number Nu, and Sherwood number Sh are defined as:

$$C_f = \frac{\tau_w}{\rho_f U_w^2} = \frac{1}{\sqrt{Re_x}}\left(1 + \frac{1}{\beta}\right)\frac{\mu_{thnf}}{\mu_f} f''(0) \tag{27}$$

$$Nu = \frac{x q_w}{k_f(T_w - T_\infty)} = -\sqrt{Re_x}\frac{k_{thnf}}{k_f}\left(1 + \frac{4}{3}R_d\right)\theta'(0) \tag{28}$$

$$Sh = \frac{x j_w}{D_f(C_w - C_\infty)} = -\sqrt{Re_x}\frac{D_{thnf}}{D_f}\phi'(0) \tag{29}$$

where $\mathrm{Re}_x = \frac{U_w x}{\nu_f}$ is the local Reynolds number, $\tau_w = \mu_{\mathrm{thnf}}\left(1 + \frac{1}{\beta}\right)\left(\frac{\partial u}{\partial y}\right)_{y=0}$ is the wall shear stress, $q_w = -k_{\mathrm{thnf}}\left(1 + \frac{4}{3}R_d\right)\left(\frac{\partial T}{\partial y}\right)_{y=0}$ is the wall heat flux, and $j_w = -D_{\mathrm{thnf}}\left(\frac{\partial C}{\partial y}\right)_{y=0}$ is the wall mass flux.

In the tables and discussion, the reduced quantities $C_f^* = \sqrt{Re_x}\, C_f \frac{\mu_f}{\mu_{thnf}} = \left(1 + \frac{1}{\beta}\right) f''(0)$, $Nu^* = -\theta'(0)$ and $Sh^* = -\phi'(0)$ are reported.

3. Solution Methodology

3.1. Perturbation Technique

Due to the strong nonlinearity of the governing Equations (12)–(14), an exact analytical solution of the complete coupled system (with slip and with the variable-coefficient energy and concentration equations) is not available, although the momentum equation alone admits a closed-form solution (Sections 3.7 and 3.7.6). Therefore, we employ the regular perturbation method to obtain an approximate analytical solution. The Casson fluid parameter β is considered to be large, and we introduce a small perturbation parameter $\epsilon = 1/\beta$.

Applicability of the large-β approximation. The expansion is an asymptotic series in $\epsilon = 1/\beta$. Because β enters Equation (12) only through the factor $(1 + \epsilon)$ multiplying the viscous term, the exact no-slip momentum solution depends on $(1 + \epsilon)^{-1/2}$ (Section 3.7.6), whose binomial expansion converges only for $|\epsilon| < 1$, i.e., $\beta > 1$. The perturbation solution is therefore used here only for $\beta > 1$; it is validated at $\beta = 1.5$ ($\epsilon \approx 0.67$, Table 2), and its truncation error, of order ϵ^3, decreases as β increases. The results for $\beta = 0.5$ and 1.0 (Table 2) are obtained exclusively from the numerical solution.

Table 2. Comparison of numerical solution (NS) and perturbation solution (PS) for $(1 + 1/\beta)f''(0)$, $-\theta'(0)$, and $-\phi'(0)$ when $\beta = 1.5$, $M = 1.0$, $\phi_1 = \phi_2 = \phi_3 = 0.01$, $R_d = 0.3$, $Q = 0.1$, $Sc = 0.6$, $K = 0.2$, $\lambda_s = \lambda_t = 0$.

Quantity	Numerical Solution (NS)	Perturbation Solution (PS)	Absolute Error	Relative Error (%)
$(1 + 1/\beta)f''(0)$	−1.40307	−1.39854	0.00453	0.32
$-\theta'(0)$	0.95646	0.95122	0.00524	0.55
$-\phi'(0)$	0.56207	0.55891	0.00316	0.56

3.2. Perturbation Expansions

The functions $f(\eta)$, $\theta(\eta)$, and $\phi(\eta)$ are expanded in power series of the small parameter ϵ as follows:

$$f(\eta) = f_0(\eta) + \epsilon f_1(\eta) + \epsilon^2 f_2(\eta) + O(\epsilon^3) \quad (30)$$

$$\theta(\eta) = \theta_0(\eta) + \epsilon\theta_1(\eta) + \epsilon^2\theta_2(\eta) + O(\epsilon^3) \quad (31)$$

$$\phi(\eta) = \phi_0(\eta) + \epsilon\phi_1(\eta) + \epsilon^2\phi_2(\eta) + O(\epsilon^3) \quad (32)$$

3.3. Zeroth-Order System ($\boldsymbol{O(\epsilon^0)}$)

Substituting the expansions (30)–(32) into Equations (12)–(14) and collecting terms of $O(\epsilon^0)$, we obtain the zeroth-order system:

3.3.1. Zeroth-Order Momentum Equation

$$A_1 f_0''' + f_0 f_0'' - (f_0')^2 - A_2 M f_0' = 0 \quad (33)$$

3.3.2. Zeroth-Order Energy Equation

$$A_3\left(1+\frac{4}{3}R_d\right)\theta_0'' + \Pr f_0\theta_0' + \Pr Q A_4\theta_0 = 0 \tag{34}$$

3.3.3. Zeroth-Order Concentration Equation

$$A_5\phi_0'' + Scf_0\phi_0' - ScK\phi_0 = 0 \tag{35}$$

3.3.4. Zeroth-Order Boundary Conditions

The zeroth-order system corresponds to the Newtonian case ($\beta \to \infty$, $\epsilon = 0$). Its boundary conditions are derived from Equations (15) and (16):

$$f_0(0) = 0, \quad f_0'(0) = 1 + \lambda_s f_0''(0), \quad \theta_0(0) = 1 + \lambda_t\theta_0'(0), \quad \phi_0(0) = 1 \tag{36}$$

$$f_0'(\infty) \to 0, \quad \theta_0(\infty) \to 0, \quad \phi_0(\infty) \to 0 \tag{37}$$

where the constant coefficients A_1 to A_5 are defined as:

$$A_1 = \frac{\mu_{\text{thnf}}/\mu_f}{\rho_{\text{thnf}}/\rho_f}, \quad A_2 = \frac{\sigma_{\text{thnf}}/\sigma_f}{\rho_{\text{thnf}}/\rho_f},$$

$$A_3 = \frac{k_{thnf}/k_f}{\left(\rho C_p\right)_{thnf}/\left(\rho C_p\right)_f}, \quad A_4 = \frac{1}{\left(\rho C_p\right)_{thnf}/\left(\rho C_p\right)_f},$$

$$A_5 = \frac{D_{thnf}}{D_f}$$

With these definitions, Equations (34) and (35) follow from Equations (13) and (14) after multiplication by Pr and Sc, respectively, so that the zeroth-order system and the first-order ODE system (70)–(76) used in the numerical method are mutually consistent.

3.4. First-Order System ($\boldsymbol{O(\epsilon^1)}$)

Collecting terms of $O(\epsilon^1)$, we obtain the first-order system:

3.4.1. First-Order Momentum Equation

$$A_1 f_1''' + f_0 f_1'' + f_1 f_0'' - 2f_0' f_1' - A_2 M f_1' = -A_1 f_0''' \tag{38}$$

3.4.2. First-Order Energy Equation

$$A_3\left(1+\frac{4}{3}R_d\right)\theta_1'' + \Pr\left(f_0\theta_1' + f_1\theta_0'\right) + \Pr Q A_4\theta_1 = 0 \tag{39}$$

3.4.3. First-Order Concentration Equation

$$A_5\phi_1'' + Sc(f_0\phi_1' + f_1\phi_0') - ScK\phi_1 = 0 \tag{40}$$

3.4.4. First-Order Boundary Conditions

The first-order system ($O(\epsilon^1)$) is subject to homogeneous boundary conditions. Differentiating the slip conditions in Equation (15) with respect to ϵ and evaluating at $\epsilon = 0$ gives:

$$f_1(0) = 0, \quad f_1'(0) = \lambda_s f_1''(0), \quad \theta_1(0) = \lambda_t \theta_1'(0), \quad \phi_1(0) = 0 \tag{41}$$

$$f_1'(\infty) \to 0, \quad \theta_1(\infty) \to 0, \quad \phi_1(\infty) \to 0 \tag{42}$$

3.5. Second-Order System ($O(\epsilon^2)$)

Collecting terms of $O(\epsilon^2)$, we obtain the second-order system:

3.5.1. Second-Order Momentum Equation

$$A_1 f_2''' + f_0 f_2'' + f_2 f_0'' + f_1 f_1'' - 2 f_0' f_2' - (f_1')^2 - A_2 M f_2' = -A_1 f_1''' \tag{43}$$

3.5.2. Second-Order Energy Equation

$$A_3\left(1 + \frac{4}{3}R_d\right)\theta_2'' + \Pr\left(f_0\theta_2' + f_2\theta_0' + f_1\theta_1'\right) + \Pr Q A_4 \theta_2 = 0 \tag{44}$$

3.5.3. Second-Order Concentration Equation

$$A_5\phi_2'' + Sc(f_0\phi_2' + f_2\phi_0' + f_1\phi_1') - ScK\phi_2 = 0 \tag{45}$$

3.5.4. Second-Order Boundary Conditions

Similarly, the second-order system ($O(\epsilon^2)$) has homogeneous boundary conditions obtained from the second derivative with respect to ϵ:

$$f_2(0) = 0, \quad f_2'(0) = \lambda_s f_2''(0), \quad \theta_2(0) = \lambda_t \theta_2'(0), \quad \phi_2(0) = 0 \tag{46}$$

$$f_2'(\infty) \to 0, \quad \theta_2(\infty) \to 0, \quad \phi_2(\infty) \to 0 \tag{47}$$

3.6. Solution of the Perturbation Equations

The zeroth-order Equations (33)–(35) represent the Newtonian fluid case ($\beta \to \infty$) and are solved first under the boundary conditions (36)–(37). The solutions $f_0(\eta)$, $\theta_0(\eta)$, and $\phi_0(\eta)$ are then substituted into the first-order Equations (38)–(40), which are solved under homogeneous boundary conditions (41)–(42). This process is repeated for the second-order system.

The final approximate solutions up to the second order are given by:

$$f(\eta) \approx f_0(\eta) + \frac{1}{\beta} f_1(\eta) + \frac{1}{\beta^2} f_2(\eta) \tag{48}$$

$$\theta(\eta) \approx \theta_0(\eta) + \frac{1}{\beta}\theta_1(\eta) + \frac{1}{\beta^2}\theta_2(\eta) \tag{49}$$

$$\phi(\eta) \approx \phi_0(\eta) + \frac{1}{\beta}\phi_1(\eta) + \frac{1}{\beta^2}\phi_2(\eta) \tag{50}$$

3.7. Zeroth-Order Solution

The zeroth-order system corresponds to the case of a Newtonian ternary hybrid nanofluid ($\beta \to \infty$). The governing equations and boundary conditions form a well-defined boundary-value problem that admits an exact solution.

3.7.1. Assumed Form of the Solution

For the flow over a linearly stretching sheet, the form of the zeroth-order stream function is well-established. We assume the following solutions, which satisfy the wall conditions (36) and the far-field conditions (37):

$$f_0(\eta) = \frac{1 - e^{-\gamma\eta}}{\gamma(1 + \lambda_s\gamma)} \tag{51}$$

$$\theta_0(\eta) = \frac{e^{-\delta\eta}}{1 + \lambda_t\delta} \tag{52}$$

$$\phi_0(\eta) = e^{-\lambda\eta} \tag{53}$$

where γ, δ, and λ are positive constants to be determined by substituting into the governing equations.

3.7.2. Zeroth-Order Velocity Field

The corresponding velocity components are:

$$f_0{}'(\eta) = \frac{e^{-\gamma\eta}}{1 + \lambda_s\gamma} \tag{54}$$

$$f_0{}''(\eta) = -\frac{\gamma e^{-\gamma\eta}}{1 + \lambda_s\gamma} \tag{55}$$

$$f_0{}'''(\eta) = \frac{\gamma^2 e^{-\gamma\eta}}{1 + \lambda_s\gamma} \tag{56}$$

Substituting these into the zeroth-order momentum Equation (33), with $c = 1/(1 + \lambda_s\gamma) = f_0{}'(0)$:

$$A_1 c\gamma^2 e^{-\gamma\eta} + \frac{c}{\gamma}(1 - e^{-\gamma\eta})(-c\gamma e^{-\gamma\eta}) - c^2 e^{-2\gamma\eta} - A_2 M c e^{-\gamma\eta} = 0$$

Simplifying and collecting terms, we obtain the characteristic equation for γ: (the terms proportional to $e^{-2\gamma\eta}$ cancel identically)

$$A_1\gamma^2(1 + \lambda_s\gamma) - A_2 M(1 + \lambda_s\gamma) - 1 = 0 \tag{57}$$

Solving for the positive non-zero root (for $\lambda_s = 0$):

$$\gamma = \sqrt{\frac{1 + A_2 M}{A_1}} \tag{58}$$

For $\lambda_s > 0$, γ is the positive real root of the cubic (57); because the coefficients of (57), written in powers of γ, change sign only once, Descartes' rule of signs guarantees that exactly one positive root exists for all $A_1, A_2, M, \lambda_s > 0$. For a particle-free Newtonian fluid ($A_1 = A_2 = 1, \lambda_s = 0$), Equation (58) gives $f''(0) = -\sqrt{1 + M}$, the classical MHD stretching-sheet result, which reduces to Crane's solution $f''(0) = -1$ for $M = 0$ [6,29].

Thus, the zeroth-order velocity solution is:

$$f_0{}'(\eta) = \frac{1}{1 + \lambda_s\gamma}\exp(-\gamma\eta), \qquad \lambda_s = 0 : f_0{}'(\eta) = \exp\left(-\sqrt{\frac{1 + A_2 M}{A_1}}\,\eta\right) \tag{59}$$

where $\kappa = f_0(\infty) = 1/[\gamma(1 + \lambda_s\gamma)]$ is the dimensionless entrainment, the normal velocity far from the sheet being $v_\infty = -\sqrt{a\nu_f}\,\kappa$. Equation (51) satisfies Equation (33) and the conditions (36)–(37) exactly.

3.7.3. Zeroth-Order Temperature Field

Substituting the assumed temperature solution (52) into the energy Equation (34):

$$A_3\left(1+\frac{4}{3}R_d\right)\delta^2 e^{-\delta\eta} - Pr\,\delta\,\frac{1-e^{-\gamma\eta}}{\gamma(1+\lambda_s\gamma)}e^{-\delta\eta} + Pr\,Q A_4 e^{-\delta\eta} = 0$$

Because this relation cannot be satisfied identically in η, the decay constant is determined from the dominant balance as $\eta \to \infty$, where $f_0 \to \kappa$ (the common factor $1/(1+\lambda_t\delta)$ has been omitted):

$$A_3\left(1+\frac{4}{3}R_d\right)\delta^2 - \kappa\,Pr\,\delta + Pr\,Q A_4 = 0 \tag{60}$$

Solving this quadratic equation:

$$\delta = \frac{\kappa Pr \pm \sqrt{\kappa^2 Pr^2 - 4A_3A_4Q\,Pr\left(1+\frac{4}{3}R_d\right)}}{2A_3\left(1+\frac{4}{3}R_d\right)} \tag{61}$$

The physically relevant solution is the positive root that ensures $\theta_0(\infty) = 0$. For a heat sink ($Q < 0$) the two roots have opposite signs and the "+" root is the only positive one; for $Q > 0$ both roots are positive, but only the "+" root remains non-zero as $Q \to 0$, where it recovers $\delta = \kappa Pr/[A_3(1+4R_d/3)]$. Real roots require a non-negative discriminant, i.e., $Q \le Q_c = \frac{\kappa^2 Pr}{4A_3A_4\left(1+\frac{4}{3}R_d\right)}$. For $Q > Q_c$ (strong internal heat generation) δ becomes complex, so that θ_0 would oscillate in η and could not represent a monotonically decaying thermal boundary layer; physically, the heat generated then exceeds the rate at which it can be removed by convection and conduction. All parameter combinations used in this study satisfy $Q < Q_c$.

3.7.4. Zeroth-Order Concentration Field

Substituting the assumed concentration solution (53) into the concentration Equation (35):

$$A_5\lambda^2 e^{-\lambda\eta} - Sc\,\lambda\,\frac{1-e^{-\gamma\eta}}{\gamma(1+\lambda_s\gamma)}e^{-\lambda\eta} - ScKe^{-\lambda\eta} = 0$$

Considering the dominant term as $\eta \to \infty$:

$$A_5\lambda^2 - \kappa\,Sc\,\lambda - ScK = 0 \tag{62}$$

Solving this quadratic equation:

$$\lambda = \frac{\kappa Sc \pm \sqrt{\kappa^2 Sc^2 + 4A_5ScK}}{2A_5} \tag{63}$$

Again, the physically relevant solution is the positive root that ensures $\phi_0(\infty) = 0$. For a destructive reaction ($K > 0$) the discriminant is always positive, and the roots have opposite signs, so exactly one positive real root exists; complex values could arise only for a strongly generative reaction with $K < -\kappa^2 Sc/(4A_5)$, which is outside the range considered here.

3.7.5. Summary of Zeroth-Order Solution

The complete zeroth-order solution is given by:

$$f_0(\eta) = \frac{1-e^{-\gamma\eta}}{\gamma(1+\lambda_s\gamma)} \tag{64}$$

$$\theta_0(\eta) = \frac{e^{-\delta\eta}}{1+\lambda_t\delta} \tag{65}$$

$$\phi_0(\eta) = e^{-\lambda\eta} \tag{66}$$

where the decay parameters are determined by:

$$\gamma = \sqrt{\frac{1 + A_2 M}{A_1}} \quad (\lambda_s = 0;\ \text{for } \lambda_s > 0,\ \text{positive root of (57)}) \tag{67}$$

$$\delta = \frac{\kappa Pr + \sqrt{\kappa^2 Pr^2 - 4A_3 A_4 Q\, Pr\left(1 + \frac{4}{3}R_d\right)}}{2A_3\left(1 + \frac{4}{3}R_d\right)} \tag{68}$$

$$\lambda = \frac{\kappa Sc + \sqrt{\kappa^2 Sc^2 + 4A_5 ScK}}{2A_5} \tag{69}$$

with A_1–A_5 as defined in Section 3.3.4 and $\kappa = 1/[\gamma(1 + \lambda_s\gamma)]$.

The velocity solution (64) satisfies Equation (33) and the boundary conditions (36)–(37) exactly. The temperature and concentration solutions (65)–(66) satisfy the wall and far-field conditions exactly, but satisfy Equations (34)–(35) only in the dominant-balance (large-η) sense; they therefore constitute an approximate analytical zeroth-order solution for the Newtonian case of the ternary hybrid nanofluid, and this approximation is one source of the small differences between the perturbation and numerical solutions in Table 2.

3.7.6. Closed-Form First- and Second-Order Momentum Corrections

For $\lambda_s = 0$ the Casson parameter enters the momentum Equation (12) only through the factor $(1 + \epsilon)$ multiplying $A_1 f'''$. Repeating the derivation of Section 3.7 with A_1 replaced by $(1 + \epsilon)A_1$ shows that Equation (12) with conditions (15)–(16) is satisfied exactly by

$$f(\eta) = \frac{1 - e^{-\gamma\eta}}{\gamma}, \qquad \gamma = \frac{\gamma_0}{\sqrt{1 + \epsilon}}, \qquad \gamma_0 = \sqrt{\frac{1 + A_2 M}{A_1}}$$

Expanding this solution in powers of ε yields the exact solutions of the first-order problem (38), (41)–(42) and of the second-order problem (43), (46)–(47):

$$f_1(\eta) = \frac{1 - (1 + \gamma_0\eta)e^{-\gamma_0\eta}}{2\gamma_0}, \qquad f_2(\eta) = -\frac{1 - \left(1 + \gamma_0\eta - \gamma_0^2\eta^2\right)e^{-\gamma_0\eta}}{8\gamma_0}$$

which can be verified by direct substitution, and which satisfy $f_i(0) = f_i'(0) = f_i'(\infty) = 0$ $(i = 1, 2)$. The Casson corrections to the wall quantities therefore appear explicitly:

$$f''(0) = -\gamma_0\left(1 - \frac{\epsilon}{2} + \frac{3\epsilon^2}{8}\right) + O(\epsilon^3), \qquad (1 + \epsilon)f''(0) = -\gamma_0\left(1 + \frac{\epsilon}{2} - \frac{\epsilon^2}{8}\right) + O(\epsilon^3)$$

The first- and second-order thermal and solutal corrections θ_1, θ_2, ϕ_1, ϕ_2 satisfy the linear non-homogeneous Equations (39)–(40) and (44)–(45), in which f_1 and f_2 above act as known forcing terms; together with Equations (48)–(50), they complete the second-order perturbation solution used in Section 6.2.

4. Numerical Method

The coupled, nonlinear boundary-value problem posed by Equations (12)–(14) subject to the boundary conditions (15)–(16) is solved using the numerical solver NDSolve in Mathematica. To facilitate this computation, the system of higher-order ODEs is first converted into a system of first-order ODEs.

4.1. System of First-Order ODEs

We introduce the following new variables:

$$y_1 = f, \quad y_2 = f', \quad y_3 = f'',$$
$$y_4 = \theta, \quad y_5 = \theta',$$
$$y_6 = \phi, \quad y_7 = \phi'$$

The system of Equations (12)–(14) is then transformed into the following set of first-order equations:

$$y_1{}' = y_2 \tag{70}$$
$$y_2{}' = y_3 \tag{71}$$
$$y_3{}' = \frac{1}{\left(1+\frac{1}{\beta}\right)A_1}\left(y_2^2 + A_2 M y_2 - y_1 y_3\right) \tag{72}$$
$$y_4{}' = y_5 \tag{73}$$
$$y_5{}' = -\frac{1}{A_3\left(1+\frac{4}{3}R_d\right)}\left(\Pr y_1 y_5 + \Pr Q A_4 y_4\right) \tag{74}$$
$$y_6{}' = y_7 \tag{75}$$
$$y_7{}' = -\frac{1}{A_5}\left(Sc\, y_1 y_7 - Sc\, K y_6\right) \tag{76}$$

4.2. Boundary Conditions for the Numerical Solution

The boundary conditions in terms of the new variables are given at the wall ($\eta = 0$) and at the edge of the boundary layer ($\eta = \eta_\infty$), where η_∞ is chosen to be a sufficiently large value where the asymptotic conditions are satisfied.

The core challenge is implementing the slip conditions at $\eta = 0$, which are now implicit. We require:

$$\text{Velocity Slip}: \quad y_2(0) = 1 + \lambda_s y_3(0)$$
$$\text{Thermal Slip}: \quad y_4(0) = 1 + \lambda_t y_5(0)$$

These cannot be directly specified as simple values. Therefore, the boundary conditions for the numerical solver are formulated as follows:

$$\text{At } \eta = 0: \quad y_1(0) = 0 \tag{77}$$
$$y_2(0) - \lambda_s y_3(0) = 1 \tag{78}$$
$$y_4(0) - \lambda_t y_5(0) = 1 \tag{79}$$
$$y_6(0) = 1 \tag{80}$$
$$\text{As } \eta \to \eta_\infty: \quad y_2(\eta_\infty) \to 0, \quad y_4(\eta_\infty) \to 0, \quad y_6(\eta_\infty) \to 0 \tag{81}$$

This formulation is crucial. The values and gradients at the boundary are involved in the linear Equations (78) and (79). Such mixed or Robin-type boundary conditions can be effectively handled by contemporary numerical solvers such as NDSolve. In order to simultaneously fulfill these boundary constraints and the differential equations, the solver iteratively finds values for $y_3(0)$ ($f''(0)$) and $y_5(0)$ ($\theta'(0)$).

Under the boundary conditions (77)–(81), the system of Equations (70)–(76) is solved numerically. The values of $f''(0)$, $\theta'(0)$, and $\phi'(0)$ obtained from this solution in Equations (27)–(29) are then used to calculate the skin friction, Nusselt number, and Sherwood number.

Numerical accuracy and reproducibility. The computations use a finite domain $0 \le \eta \le \eta_\infty$, and the solver tolerances (AccuracyGoal/PrecisionGoal) are set; increasing η_∞ further changes the wall gradients by less. The present study is a deterministic boundary-value computation that involves no data-driven model and no training, validation, or testing split; repeated runs therefore give identical results, and the accuracy is quantified instead against the closed-form momentum solution (Section 3.7.6: the values of C_f^* in Table 1 follow the predicted $\sqrt{1 + 1/\beta}$ scaling to within about 10^{-4} in relative terms) and against the perturbation solution (Table 2).

5. Results and Discussion

Using graphical representations, the flow, thermal, and concentration properties of a ternary hybrid nanofluid (Al_2O_3-Cu-TiO_2/water) on a stretched surface are thoroughly examined. The impacts of important physical parameters on concentration, temperature, and velocity profiles are shown in this section, and the underlying physical mechanisms are then thoroughly discussed.

5.1. Velocity Profiles

Figures 2–4 display the dimensionless stream function $f(\eta)$, whose slope $f'(\eta) = u/(ax)$ is the dimensionless velocity and whose asymptotic value $f(\infty) = \kappa$ measures the entrainment of ambient fluid towards the sheet; a smaller asymptotic value therefore corresponds to a faster-decaying velocity and a thinner momentum boundary layer.

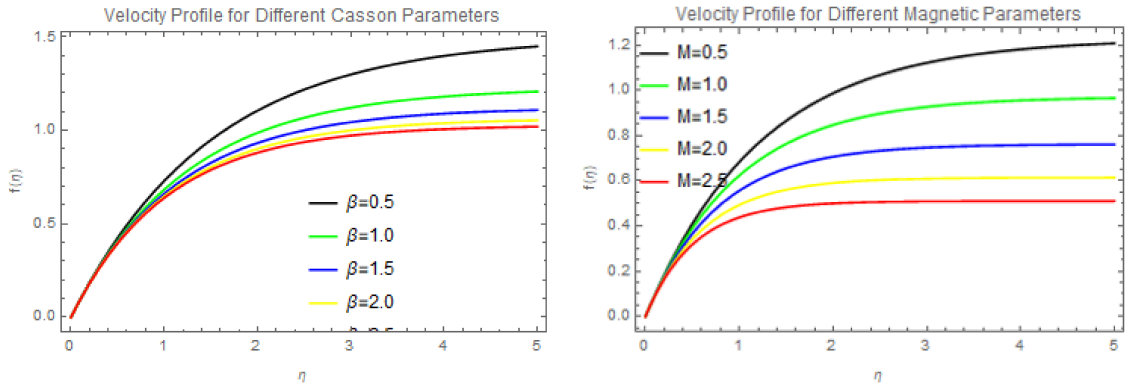

(**a**) (**b**)

Figure 2. (**a**) Velocity profiles for various values of the Casson parameter β (**b**) Velocity profiles for various values of the magnetic parameter M.

Different physical characteristics have different effects on the velocity profiles. The velocity boundary layer thickness decreases when the Casson parameter β is increased from 0.5 to 2.5, as seen in Figure 2a, suggesting a shift toward more Newtonian behavior with a lower effective viscosity, a faster decay of the velocity (larger γ), and a smaller wall shear stress (Table 1). Magnetic fields (M increasing from 0.5 to 2.5) suppress fluid motion because of Lorentz force opposition, as seen in Figure 2b, significantly lowering velocity profiles. Because the momentum Equation (12) contains no buoyancy term, it is decoupled from the energy and concentration equations; consequently, the radiation parameter R_d (Figure 3a), the heat source parameter Q (Figure 3b), the Schmidt number Sc (Figure 4a), and the chemical reaction parameter K (Figure 4b) leave the velocity field unchanged. The coincident curves in Figures 3 and 4 confirm this one-way coupling and provide a consistency check of the numerical solution.

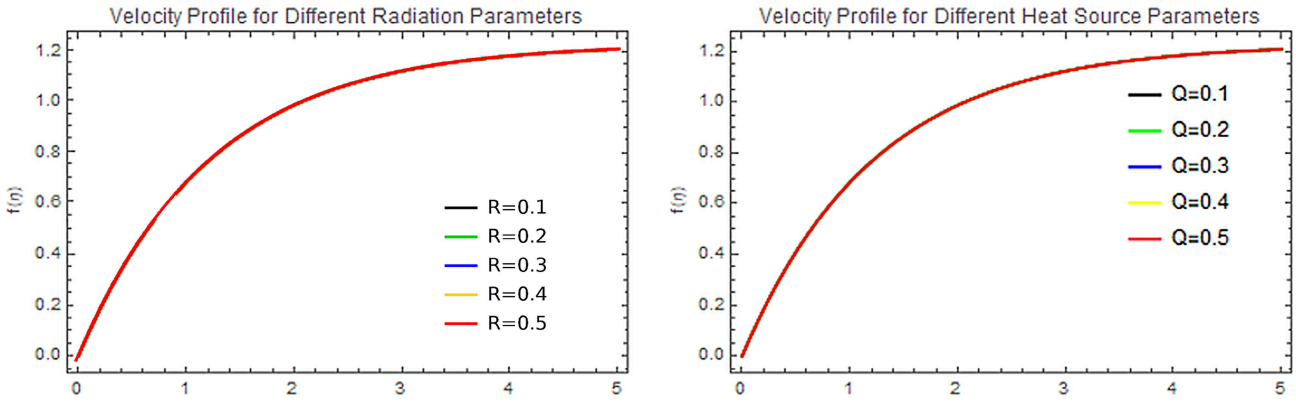

(**a**) (**b**)

Figure 3. (**a**) Velocity profiles for various values of the radiation parameter R_d (**b**) Velocity profiles for various values of the heat source parameter Q.

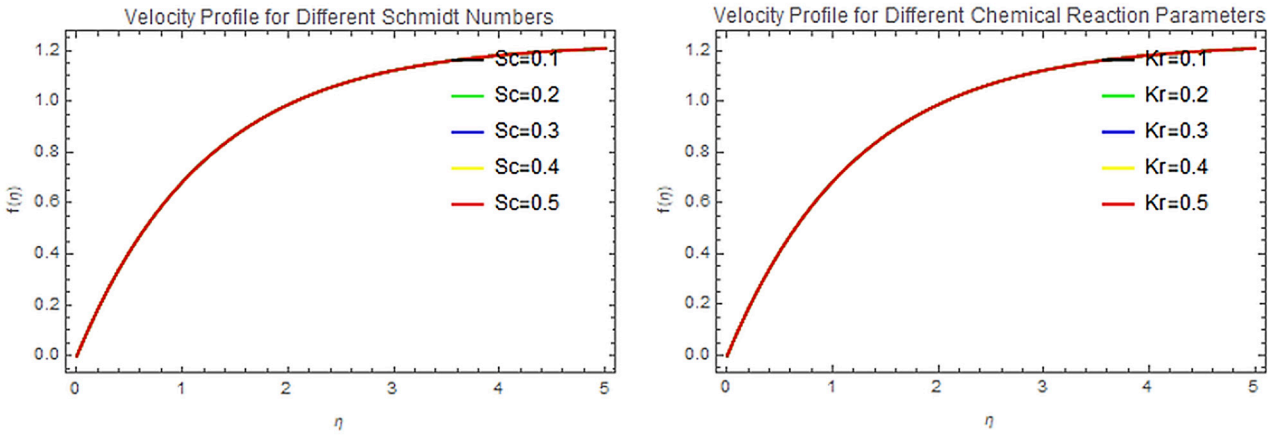

(**a**) (**b**)

Figure 4. (**a**) Velocity profiles for various Schmidt numbers Sc (**b**) Velocity profiles for various chemical reaction parameters K.

5.2. Temperature Profiles

The results indicate that as the values of the Casson and magnetic parameters increase, the temperature distribution and thermal boundary layer thickness increase. As the Casson number increases, the thermal boundary layer will thicken because the faster-decaying velocity field entrains less ambient fluid (smaller $\kappa = f_0(\infty)$), which weakens the convective transport of heat away from the wall (Figure 5a); this is consistent with the decrease of $-\theta'(0)$ in Table 1. The increase in the magnetic parameter likewise raises the temperature (Figure 5b), because the Lorentz drag decelerates the flow and reduces the convective heat removal; Joule heating is not included in the energy Equation (3) and therefore does not contribute to this effect. The radiation parameter produces the most significant increase in the temperature distribution across the thermal boundary layer due to increased radiative heat transfer (Figure 6a). The heat source parameter generates temperature increases within the thermal boundary layer by creating an internal heat source (Figure 6b). The Schmidt number (Figure 7a) and chemical reaction parameter (Figure 7b) leave the temperature distribution unchanged, because the energy Equation (13) does not contain the concentration field.

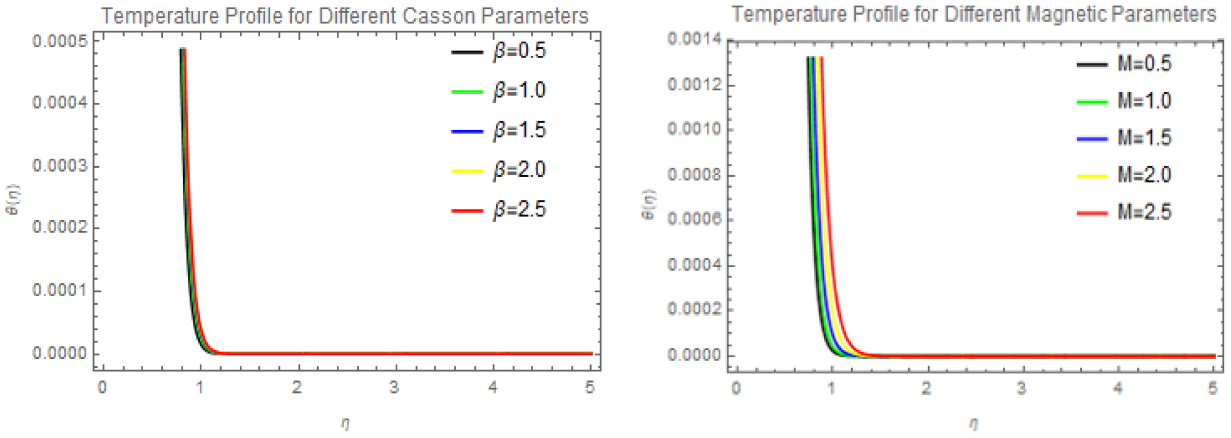

(**a**) (**b**)

Figure 5. (**a**) Temperature profiles for various values of the Casson parameter β (**b**) Temperature profiles for various values of the magnetic parameter M.

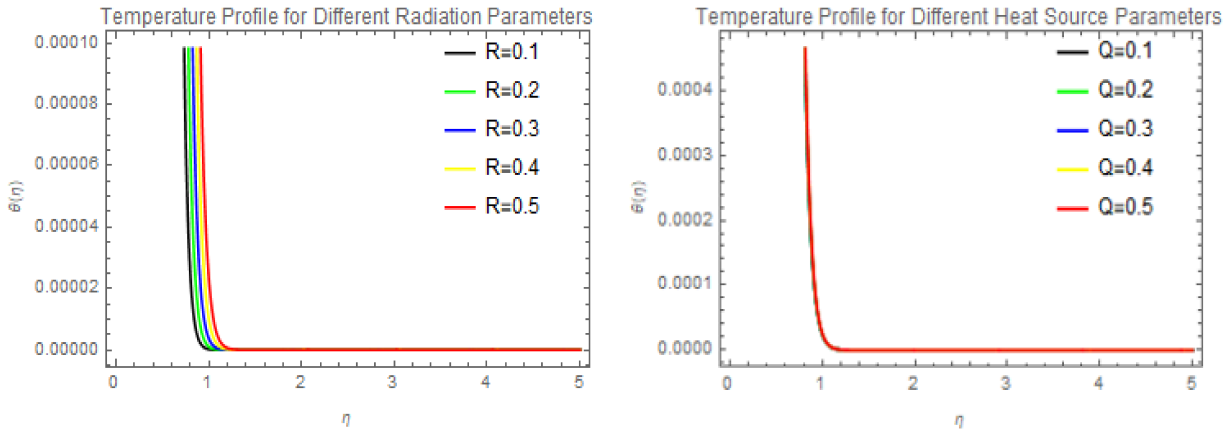

(**a**) (**b**)

Figure 6. (**a**) Temperature profiles for various values of the radiation parameter R_d (**b**) Temperature profiles for various values of the heat source parameter Q.

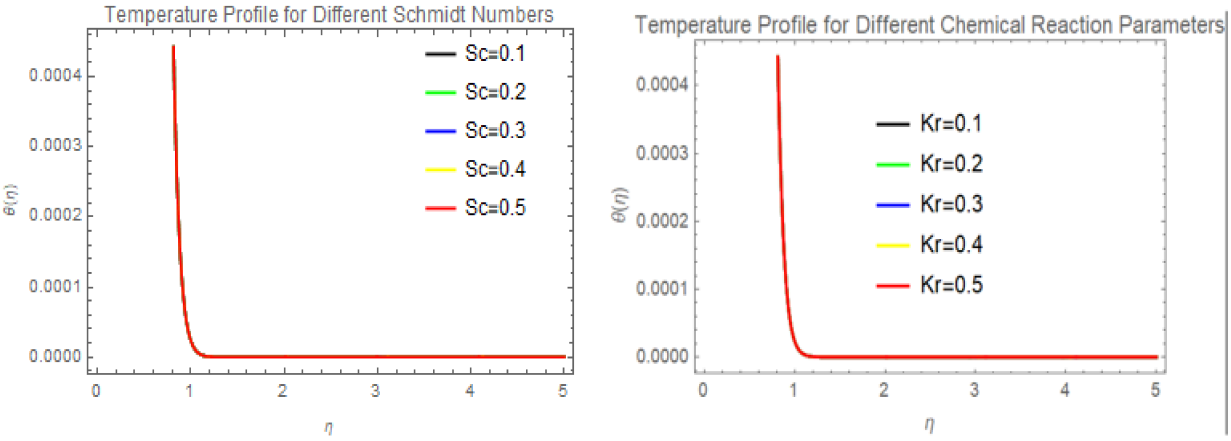

(**a**) (**b**)

Figure 7. (**a**) Temperature profiles for various values of the Schmidt number Sc (**b**) Temperature profiles for various values of the chemical reaction parameter K.

5.3. Concentration Profiles

The results of concentration profiles exhibit various trends based on the parameters examined. Like the effect of temperature, an increase in the Casson parameter slightly thickens the concentration boundary layer (Figure 8a), consistent with the decrease of $-\phi'(0)$ in Table 1, while the increase in concentration with the magnetic parameter (Figure 8b) results from the weaker convective transport of species by the decelerated flow. The radiation (Figure 9a) and heat source (Figure 9b) parameters do not influence the concentration profile, because the concentration Equation (14) contains neither the temperature nor temperature-dependent source terms; the curves in Figure 9 therefore coincide. The most pronounced shift in the concentration boundary layer exists within the Schmidt number (Figure 10a), with an increase in this parameter thinning the concentration boundary layer due to the reduced rate of mass diffusion within the liquid. The effect of increasing chemical reaction rate (Figure 10b) has an opposite relationship with concentration, as increased rates of chemical reaction will significantly deplete or reduce concentrations due to the increased consumption of substances within a chemical reaction.

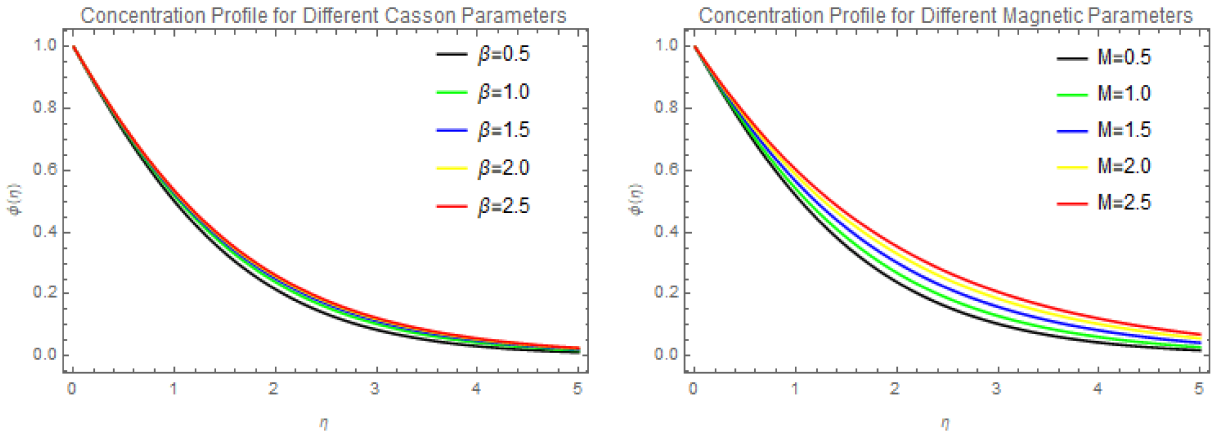

(**a**) (**b**)

Figure 8. (**a**) Concentration profiles for various values of the Casson parameter β (**b**) Concentration profiles for various values of the magnetic parameter M.

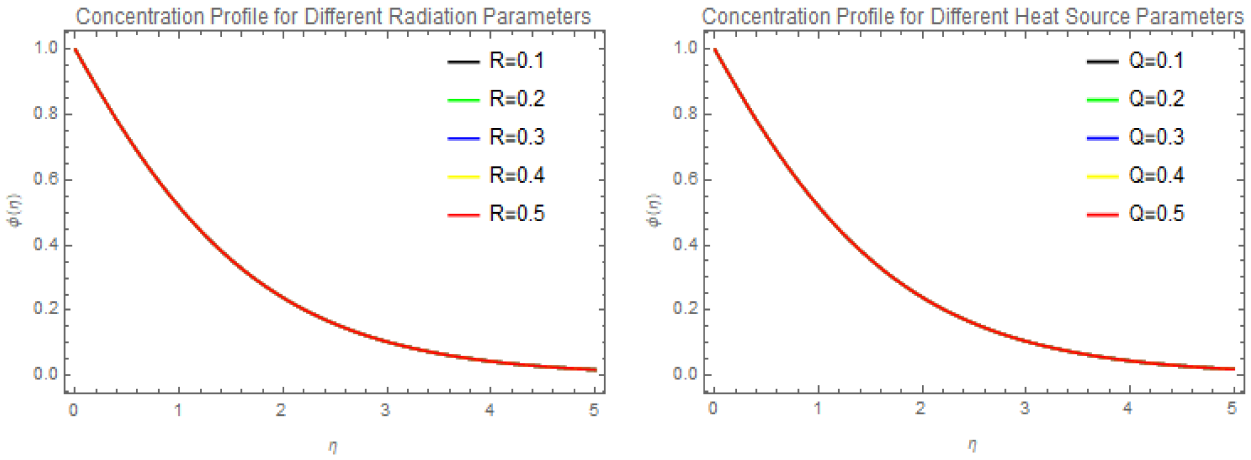

(**a**) (**b**)

Figure 9. (**a**) Concentration profiles for various values of the radiation parameter R_d (**b**) Concentration profiles for various values of the heat source parameter Q.

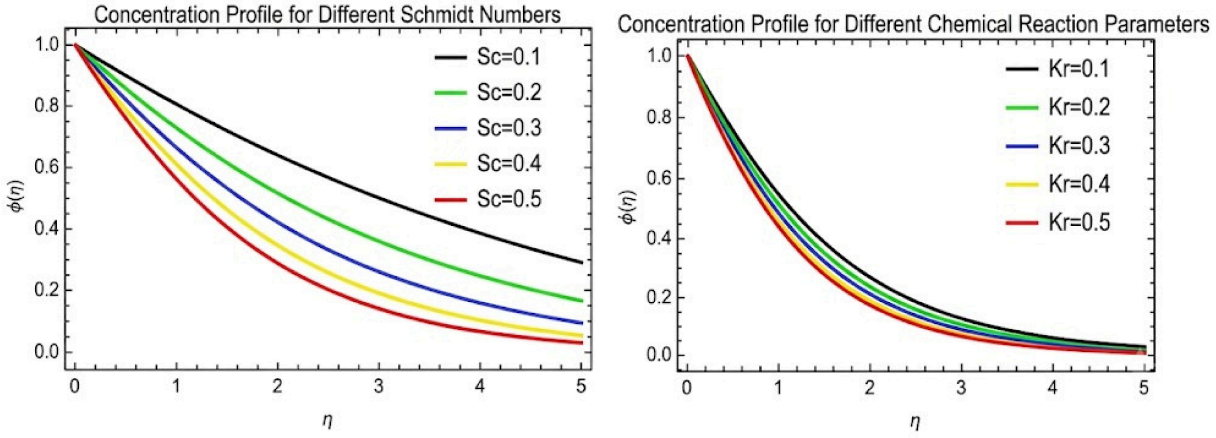

(**a**) (**b**)

Figure 10. (**a**) Concentration profiles for various Schmidt numbers *Sc* (**b**) Concentration profiles for various chemical reaction parameters *K*.

5.4. Discussion

These trends can be explained in relation to the physical principles governing heat transfer and fluid flow dynamics. In relation to the non-Newtonian flow characteristics of a yield-stressed fluid (where yield stress limits the ability of a fluid to move), it is logical that as the Casson model is adjusted, the velocity of a fluid will drop relative to the rise in yield stress (drop in fluid velocity). The improvements made to the temperature profile support this relationship by creating the condition where lower flow velocities allow for increased accumulation of thermal energy within the boundary layer.

The magnetic field effects are easily demonstrated through classic magnetohydrodynamics, where induced electric currents create magnetic forces (Lorentz forces) opposing the movement of the liquid, raising concentrations and temperature but lowering the velocity of the liquid. This has major implications for industries that utilize magnetic fields to influence the characteristics of heat and flow within their processes.

By studying the temperature profiles (Figure 6a), we can see how much of an effect radiation has on the behavior of the temperature profile. Whereas radiation does not significantly influence the transfer of momentum within the medium, it plays a large role in transferring heat energy and is an essential mechanism for delivering energy at high temperatures, as a result of our velocity profiles changing relatively little due to radiation.

The internal heat generation significantly increases the temperature of the fluid; because buoyancy is not included in the present momentum equation, the velocity field is unaffected (Figure 3b), and a buoyancy-driven enhancement of the flow would require a mixed-convection extension of the model. Therefore, applications that require either electrical heating or exothermic reactions will benefit from this finding.

The Schmidt number effect demonstrates the differences in the way that mass is transferred compared to momentum and heat. The sensitivity of the concentration boundary layer to variations in the Schmidt number further highlights the need for the mass diffusivity data to accurately predict how species disperse.

Reaction kinetics play a critical role in mass transfer processes. The chemical reaction parameter has a considerable effect on concentration profiles, while it has no effect on the temperature and velocity profiles in the present one-way coupled model. This implies that while chemical reactions affect how much of a species is in a location, they do not alter the flow and thermal characteristics of the fluid significantly.

5.5. Mechanistic Interpretation Based on the Closed-Form Momentum Solution

The closed-form solution of Sections 3.7 and 3.7.6 provides a mechanistic explanation of the trends in Figures 2–10 that goes beyond a description of the curves. For $\lambda_s = 0$ the momentum Equation (12) is satisfied exactly by $f(\eta) = [1 - \exp(-\gamma\eta)]/\gamma$ with

$$\gamma = \sqrt{\frac{1 + A_2 M}{(1 + 1/\beta)A_1}}$$

Three consequences follow. First, the Casson parameter, the magnetic field, and the nanoparticle loading act on the flow only through the single decay rate γ: a Casson ternary hybrid nanofluid with parameters (β, M) is dynamically equivalent to a Newtonian ternary hybrid nanofluid with the effective viscosity ratio $(1 + 1/\beta)A_1$. Increasing β or M increases γ, which thins the momentum boundary layer (thickness of order $1/\gamma$) and reduces the entrainment $\kappa = 1/\gamma$.

Second, the reduced skin friction is $C_f^* = (1 + 1/\beta)f''(0) = -\sqrt{(1 + 1/\beta)(1 + A_2 M)/A_1}$. Its dependence on β is therefore the universal factor $\sqrt{1 + 1/\beta}$, independent of M and of the nanoparticle volume fractions. This explains quantitatively the 31.7% reduction reported in Section 6.2 for an increase in β from 0.5 to 2.5, since $1 - \sqrt{1.4/3} = 0.317$ and the numerical values in Table 1 follow this scaling to within about 10^{-4} (relative), which constitutes an independent check of the numerical solution. A less obvious consequence is that, although the wall shear stress decreases as β increases, the wall velocity gradient $|f''(0)| = \gamma$ increases, because the reduction in the effective viscosity outweighs the steepening of the velocity profile.

Third, because the energy and concentration equations contain f only through the convective terms $f\theta'$ and $f\phi'$, the reduction in κ with increasing β or M weakens the convective supply of ambient fluid towards the wall and thereby thickens the thermal and concentration boundary layers. This is why the Casson and magnetic parameters, which act directly only on the momentum equation, decrease $-\theta'(0)$ and $-\phi'(0)$ (Table 1), whereas the purely thermal (R_d, Q) and purely solutal (Sc, K) parameters act only on their own fields.

6. Skin Friction, Nusselt Number, and Sherwood Number

6.1. Analysis of Physical Parameters

Important information about the flow, heat transfer, and mass transfer properties of the ternary hybrid nanofluid system is provided by the calculated values of the skin friction coefficient (C_f), Nusselt number (Nu), and Sherwood number (Sh) for changing Casson fluid parameter (β).

6.2. Validation and Method Comparison

By comparing the results of the applied perturbation solution (PS) with the numerical solution (NS) found using Mathematica's NDSolve function, the accuracy of the PS is verified. The validity and accuracy of the perturbation technique for the selected range of parameters are confirmed by the high agreement between the two sets of results. The perturbative technique, which truncates the infinite series solution after the second order, is what causes the small variations that are shown. High trust in the results and discussions offered is made possible by this significant correlation.

Composition of the perturbation solution. The PS values in Table 2 are evaluated from the complete second-order expansions (48)–(50); that is, they contain the zeroth-order (Newtonian) solution of Section 3.7 together with the first- and second-order Casson corrections obtained from Equations (38)–(47), so that, for example, $f''(0) \approx f_0''(0) + \epsilon f_1''(0) + \epsilon^2 f_2''(0)$ with $\epsilon = 1/\beta = 2/3$ at $\beta = 1.5$. For the momentum field, these corrections

are available in closed form (Section 3.7.6); without them, the PS would reduce to the Newtonian solution and could not capture the Casson effect.

Origin of the small differences and accuracy of the PS. The absolute differences between the NS and the PS in Table 2 are below 5.3×10^{-3} and the relative differences are 0.32–0.56%. They arise from two sources: (i) the truncation of the series (30)–(32) after the second order, the leading neglected term being of order ϵ^3, and (ii) the dominant-balance approximation used for the zeroth-order temperature and concentration fields (Section 3.7), which may explain why the differences for $-\theta'(0)$ and $-\phi'(0)$ are slightly larger than for the skin friction. Both errors decrease as β increases, because $\varepsilon = 1/\beta$ decreases; conversely, the PS should not be used for $\beta \leq 1$, where the expansion in ε does not converge (Section 3.1). Within its range of validity, the PS therefore verifies the numerical solution to within a few tenths of a percent.

As the Casson parameter increases, the magnitude of the reduced skin friction coefficient clearly exhibits a declining tendency:

- $\beta = 0.5$: $C_f^* = -1.883$
- $\beta = 2.5$: $C_f^* = -1.286$

As β rises from 0.5 to 2.5, this indicates a **31.7% reduction** in skin friction. The direction of shear stress at the wall, which resists the fluid motion, is shown by the negative numbers. The fluid becomes less resistant to flow as it approaches Newtonian behavior (higher β values), according to the decreasing size of C_f^* with rising β. Since lower yield stress effects are associated with larger β values, which facilitate easier fluid flow over the stretching surface, this is physically consistent. This reduction is exactly the factor $1 - \sqrt{1.4/3} = 0.317$ predicted by the closed-form solution (Section 5.5), which is independent of the magnetic parameter and of the nanoparticle loading.

6.3. Comparison with Benchmark Solutions and Published Studies

In the limit of a particle-free Newtonian fluid ($\phi_1 = \phi_2 = \phi_3 = 0$, so that $A_1 = A_2 = 1$; $\beta \to \infty$; $\lambda_s = 0$), the present formulation reduces to $f''(0) = -\sqrt{1+M}$, the classical result for MHD flow over a linearly stretching sheet, which is the Newtonian ($n = 1$) case of Andersson et al. [29] and reduces to Crane's exact solution $f''(0) = -1$ [6] for M = 0. The closed-form solution (58) reproduces these benchmarks exactly, and the numerical values of Table 1 follow the same closed-form Casson scaling to within about 10^{-4}. In the corresponding thermal limit ($\phi_i = 0$, $\beta \to \infty$, $M = R_d = Q = 0$, $\lambda_t = 0$), Equation (13) reduces to the regular-fluid problem of Khan and Pop [13]; [Computed $-\theta'(0)$ for Pr = 0.7, 2 and 7 and compare them with those tabulated in [13]. The qualitative trends obtained here also agree with recent studies: the magnetic field decelerates the flow and thickens the thermal and concentration boundary layers, as reported for MHD hybrid nanofluid flow over a stretching cylinder [34], and the concentration decreases with increasing Schmidt number while the temperature increases with the radiation parameter, as reported for Darcy–Forchheimer nanofluid flow over a Riga plate [35].

7. Conclusions

Understanding coupled momentum, heat, and mass transport is essential for designing industrial thermal systems and materials-processing operations in which non-Newtonian rheology and applied magnetic fields play a central role. Casson hybrid nanofluids provide a practical means to enhance thermal performance while retaining the yield-stress and shear-thinning behavior characteristic of many engineering fluids. An applied transverse magnetic field further enables active control of boundary layer flow, making simultaneous prediction of velocity, temperature, and concentration fields critical for process reliability.

This study therefore addresses the need for coupled momentum-thermal-mass control in Casson ternary hybrid nanofluid flow over stretching surfaces subject to a magnetic field.

The main findings are summarized below in terms of (a) the scientific contributions, (b) the practical implications for thermal systems, and (c) the limitations of the study.

(a) Main scientific contributions. (i) A coupled momentum–heat–mass transfer model for steady two-dimensional flow of a Casson Al_2O_3–Cu–TiO_2/water ternary hybrid nanofluid over a stretching surface with velocity and thermal slip, a transverse magnetic field, thermal radiation, heat generation/absorption, and a first-order chemical reaction has been formulated and solved numerically, and the numerical solution has been verified by a second-order perturbation expansion in $\varepsilon = 1/\beta$, with differences of 0.32–0.56% at $\beta = 1.5$ (Table 2). (ii) The momentum problem admits a closed-form solution, which shows that β, M, and the nanoparticle loading act through a single decay rate γ; consequently, the reduced skin friction scales as $\sqrt{1 + 1/\beta}$, and the 31.7% reduction obtained when β increases from 0.5 to 2.5 is independent of M and of the nanoparticle volume fractions. (iii) Increasing β or M reduces the entrainment of ambient fluid, which thickens the thermal and concentration boundary layers and lowers the reduced Nusselt and Sherwood numbers (from 0.969 to 0.952 and from 0.592 to 0.553, respectively, for $\beta = 0.5 \rightarrow 2.5$). (iv) Owing to the one-way coupling of the model, the radiation and heat source parameters affect only the temperature field, and the Schmidt number and reaction parameter affect only the concentration field; thermal radiation and internal heat generation raise the temperature, whereas larger Sc and K thin the concentration boundary layer.

(b) Practical implications for thermal systems. In materials-processing operations such as polymer extrusion, wire drawing and coating, in which a sheet is stretched through a yield-stress nanofluid, the results indicate that the magnetic field strength and the fluid rheology can be used to tune the wall shear stress and the wall heat and mass transfer rates. The universal $\sqrt{1 + 1/\beta}$ scaling provides a quick estimate of the drag penalty associated with the yield stress of the working fluid, and the fact that radiation and internal heating change the temperature field without changing the flow field allows the hydrodynamic and thermal design to be decoupled within the range of validity of the model.

(c) Limitations. (i) The model is restricted to steady, two-dimensional, laminar flow with constant properties and neglects buoyancy, viscous dissipation, and Joule heating, so that the thermal feedback on the flow is not captured. (ii) The effective properties are computed from classical correlations for dilute suspensions of spherical particles, without particle-shape, interfacial-layer, Brownian-motion, or thermophoresis effects. (iii) The perturbation solution is formally restricted to $\beta > 1$, and the zeroth-order temperature and concentration fields are dominant-balance approximations. (iv) The results have not yet been validated experimentally.

Future work and testable hypothesis. The analysis yields a measurable prediction: for a fixed magnetic parameter and nanoparticle loading, the wall shear stress of a Casson ternary hybrid nanofluid over a stretching surface should scale as $\sqrt{1 + 1/\beta}$, whereas the reduced Nusselt number should decrease only weakly (by about 2% for $\beta = 0.5 \rightarrow 2.5$). This hypothesis can be tested by drag and heat-flux measurements on a moving belt or extruded sheet using suspensions of different yield stress. Future work should also include buoyancy, viscous dissipation and Joule heating, nanoparticle shape and temperature-dependent properties, a systematic study of the slip parameters, unsteady and three-dimensional stretching, and experimental validation of the predicted trends.

Author Contributions: Conceptualization, J.V.T. and C.B.K.; Methodology, J.V.T.; Software, M.M.B.; Validation, R.V.R.; Formal analysis, R.V.R.; Investigation, M.M.B. and M.D.; Resources, A.R.; Data curation, A.R.; writing—original draft preparation, J.V.T.; Writing—review & editing, C.B.K.; Visual-

ization, M.D.; Supervision, C.B.K. All authors have read and agreed to the published version of the manuscript.

Funding: This research received no external funding.

Institutional Review Board Statement: Not applicable.

Data Availability Statement: All data supporting this are from previously published studies, which have been appropriately cited.

Acknowledgments: This work was accomplished through the substantial contributions of many collaborators, to whom the authors express sincere gratitude. The authors utilized Grammarly and QuillBot (Ver. 4.124.1) to enhance their sentence structure, grammar, and spelling while preparing this work. These tools did not produce any ideas, content, or analyses. The authors are fully responsible for the content of this work and have evaluated and edited all suggestions.

Conflicts of Interest: The authors declare no conflicts of interest.

Nomenclature

Symbol	Description (Unit)
a	stretching-rate constant of the sheet, $U_w = ax$ (s^{-1})
$A_1, \ldots, A_5$	property coefficients defined in Section 3.3.4 (–)
B_0	strength of the applied transverse magnetic field (T)
C, C_w, C_∞	species concentration in the boundary layer, at the wall and in the ambient fluid (mol m^{-3})
C_f, C_f^*	skin friction coefficient, Equation (27), and its reduced form $(1 + 1/\beta)f''(0)$ (–)
C_p	specific heat at constant pressure (J kg^{-1} K^{-1})
D	mass diffusivity (m^2 s^{-1})
f	dimensionless stream function (–)
k, k^*	thermal conductivity (W m^{-1} K^{-1}); mean absorption coefficient (m^{-1})
K_r, K	chemical reaction rate (s^{-1}); dimensionless reaction parameter $K = K_r/a$ (–)
L_s, L_t	velocity and thermal slip lengths (m)
M	magnetic parameter (–)
Nu, Sh	local Nusselt and Sherwood numbers (–)
Pr, Sc	Prandtl and Schmidt numbers of the base fluid (–)
Q_0, Q	heat generation/absorption coefficient (W m^{-3} K^{-1}); dimensionless heat source parameter (–)
q_r, q_w, j_w	radiative heat flux, wall heat flux (W m^{-2}); wall mass flux (mol m^{-2} s^{-1})
R_d	radiation parameter (–)
Re_x	local Reynolds number (–)
T, T_w, T_∞	temperature in the boundary layer, at the wall and in the ambient fluid (K)
u, v	velocity components along x and y (m s^{-1})
x, y	coordinates along and normal to the sheet (m)
α_f	thermal diffusivity of the base fluid (m^2 s^{-1})
β	Casson fluid parameter, $\beta = \mu_B\sqrt{2\pi_c}/p_y$ (–)
ϵ	perturbation parameter, ε = 1/β (–)
γ, δ, λ, κ	decay constants of the zeroth-order solution; entrainment $\kappa = f_0(\infty)$ (–)
η	similarity variable (–)
θ, ϕ	dimensionless temperature and concentration (–)
ϕ_1, ϕ_2, ϕ_3	volume fractions of Al_2O_3, Cu and TiO_2 nanoparticles (–)
λ_s, λ_t	dimensionless velocity and thermal slip parameters (–)
μ, ν	dynamic viscosity (Pa s); kinematic viscosity (m^2 s^{-1})
ρ, σ	density (kg m^{-3}); electrical conductivity (S m^{-1})
σ^*	Stefan–Boltzmann constant (W m^{-2} K^{-4})
τ_w, ψ	wall shear stress (Pa); stream function (m^2 s^{-1})
Subscripts	
f	base fluid (water)
nf, hnf, $thnf$	Al_2O_3 nanofluid, Al_2O_3–Cu hybrid nanofluid and Al_2O_3–Cu–TiO_2 ternary hybrid nanofluid
$s1$, $s2$, $s3$	Al_2O_3, Cu and TiO_2 nanoparticles
w, ∞	condition at the wall and in the ambient fluid

Appendix A. Thermophysical Properties

Table A1 lists the thermophysical properties of the base fluid and of the nanoparticles used in Equations (17)–(26). The base fluid is water with $Pr = 0.7$, and the volume fractions are $\phi_1 = \phi_2 = \phi_3 = 0.01$ (Al_2O_3, Cu and TiO_2, respectively) unless stated otherwise.

Table A1. Thermophysical properties of water and of the Al_2O_3, Cu and TiO_2 nanoparticles (ρ, C_p and k from Ref. [41]).

Property	Water (f)	Al_2O_3	Cu	TiO_2
ρ (kg m^{-3})	997.1	3970	8933	4250
C_p (J kg^{-1} K^{-1})	4179	765	385	686.2
k (W m^{-1} K^{-1})	0.613	40	400	8.9538
Volume fraction	–	$\phi_1 = 0.01$	$\phi_2 = 0.01$	$\phi_3 = 0.01$

References

1. Khan, W.A.; Pop, I. Boundary-layer flow of a nanofluid past a stretching sheet. *Int. J. Heat Mass Transf.* **2010**, *53*, 2477–2483. [CrossRef]
2. Sundar, L.S.; Sharma, K.V.; Singh, M.K.; Sousa, A.C.M. Hybrid nanofluids preparation, thermal properties, heat transfer and friction factor—A review. *Renew. Sustain. Energy Rev.* **2017**, *68*, 185–198. [CrossRef]
3. Sarkar, J.; Ghosh, P.; Adil, A. A review on hybrid nanofluids: Recent research, development and applications. *Renew. Sustain. Energy Rev.* **2015**, *43*, 164–177. [CrossRef]
4. Alshuhail, K.A.; Shaik, F.; Kumar, K.A. Thermal management in microelectronics using advanced cooling technologies. *J. Electron. Packag.* **2023**, *145*, 031012.
5. Choi, S.U.S.; Eastman, J.A. Enhancing thermal conductivity of fluids with nanoparticles. In Proceedings of the ASME International Mechanical Engineering Congress and Exposition, San Francisco, CA, USA, 12–17 November 1995; p. 66.
6. Devendiran, D.K.; Amirtham, V.A. A review on preparation, characterization, properties and applications of nanofluids. *Renew. Sustain. Energy Rev.* **2016**, *60*, 21–40. [CrossRef]
7. Ashraf, M.U.; Hussain, A.; Ali, A. Recent advances in ternary hybrid nanofluids: Preparation and applications. *J. Mol. Liq.* **2022**, *368*, 120745.
8. Elsayed, A.M.; Alqahtani, S.; Khan, S.A. Thermophysical properties of ternary hybrid nanofluids: A comprehensive review. *Int. J. Heat Mass Transf.* **2023**, *215*, 124456.
9. Sahoo, R.R. Comparative thermal performance analysis of mono, hybrid and ternary nanofluids: An experimental study. *Int. Commun. Heat Mass Transf.* **2021**, *126*, 105468.
10. Sharma, P.; Gupta, M.; Kumar, R. Experimental investigation of thermal conductivity and viscosity of ternary hybrid nanofluids. *J. Therm. Anal. Calorim.* **2023**, *148*, 2345–2362. [CrossRef]
11. Jamil, M.F.; Ahmad, S.; Ali, H.M. Synthesis methods and characterization of ternary hybrid nanofluids: A state-of-the-art review. *J. Therm. Anal. Calorim.* **2022**, *147*, 5123–5145.
12. Adun, H.; Wole-Osho, I.; Okonkwo, E.C.; Kavaz, D.; Asif, M. A critical review of the preparation, stability, and thermophysical properties of ternary hybrid nanofluids. *Nanotechnol. Rev.* **2021**, *10*, 134–157.
13. Toghraie, D.; Chaharsoghi, V.A.; Afrand, M. Measurement of thermal conductivity of ZnO–TiO_2/EG hybrid nanofluid: Effects of temperature and nanoparticles concentration. *J. Therm. Anal. Calorim.* **2020**, *140*, 1245–1255. [CrossRef]
14. Hatami, M. Nanoparticles migration around the heated cylinders during the RSM optimization of a wavy-wall enclosure. *Adv. Powder Technol.* **2017**, *28*, 890–899. [CrossRef]
15. Casson, N. A flow equation for pigment-oil suspensions of the printing ink type. In *Rheology of Disperse Systems*; Mill, C.C., Ed.; Pergamon Press: Oxford, UK, 1959; pp. 84–104.
16. Reddy, G.J.; Kumar, M.; Kethireddy, B. Casson fluid flow over a vertical cone with non-uniform heat source/sink and chemical reaction. *Int. J. Ambient Energy* **2020**, *41*, 891–900.
17. Akbar, N.S.; Nadeem, S.; Haq, R.U.; Khan, Z.H. Radiation effects on MHD stagnation point flow of nano fluid towards a stretching surface with convective boundary condition. *Chin. J. Aeronaut.* **2013**, *26*, 1389–1397. [CrossRef]
18. Crane, L.J. Flow past a stretching plate. *Z. Angew. Math. Phys.* **1970**, *21*, 645–647. [CrossRef]
19. Andersson, H.I.; Bech, K.H.; Dandapat, B.S. Magnetohydrodynamic flow of a power-law fluid over a stretching sheet. *Int. J. Non-Linear Mech.* **1992**, *27*, 929–936. [CrossRef]

20. Bachok, N.; Ishak, A.; Pop, I. Boundary-layer flow of nanofluids over a moving surface in a flowing fluid. *Int. J. Therm. Sci.* **2010**, *49*, 1663–1668. [CrossRef]
21. Almeida, F.; Lopes, A.M.; Ferreira, A.M. Boundary slip effects in microchannels: A review. *Micromachines* **2019**, *10*, 523.
22. Zainal, N.A.; Nazar, R.; Naganthran, K.; Pop, I. Stability analysis of MHD hybrid nanofluid flow over a stretching/shrinking sheet with quadratic velocity. *Int. J. Numer. Methods Heat Fluid Flow* **2021**, *31*, 2564–2588.
23. Jyothi, K.; Reddy, P.S.; Reddy, M.S. Influence of velocity and thermal slip conditions on MHD Casson nanofluid flow over a stretching sheet. *Mater. Today Proc.* **2021**, *45*, 215–221.
24. Alkhaled, M.; Al-Shibani, F.; Al-Sarkhi, A. Thermal slip effects on nanofluid flow in microchannels: Analytical and numerical investigation. *Case Stud. Therm. Eng.* **2022**, *32*, 101892.
25. Shah, N.A.; Animasaun, I.L.; Ibraheem, R.O.; Babatunde, H.A.; Sandeep, N.; Pop, I. Scrutinization of the effects of Grashof number on the flow of different fluids driven by convection over various surfaces. *J. Mol. Liq.* **2021**, *329*, 115545.
26. Reddy, P.S.; Sreedevi, P.; Chamkha, A.J. Heat and mass transfer analysis of Casson hybrid nanofluid flow over a stretching sheet with chemical reaction. *J. Therm. Anal. Calorim.* **2021**, *146*, 1289–1302.
27. Gowda, R.P.; Kumar, R.; Prasannakumara, B.C. Effect of slip conditions on Casson nanofluid flow over a stretching sheet with thermal radiation. *Heat Transf.* **2021**, *50*, 3456–3475. [CrossRef]
28. Megahed, A.M. Improvement of heat transfer mechanism through a Maxwell fluid flow over a stretching sheet embedded in a porous medium with convective boundary condition and slip velocity. *J. Cent. South Univ.* **2020**, *27*, 1205–1216.
29. Lund, L.A.; Omar, Z.; Khan, I. Stability analysis of dual solutions in slip flow regime: A critical review. *Symmetry* **2020**, *12*, 748.
30. Arif, K.; Saeed, S.T.; Riaz, M.B.; Kallel, M. Artificial intelligence-based simulation of heat and mass transfer in magnetic hybrid nanofluids: An engineering application. *Case Stud. Therm. Eng.* **2026**, *82*, 108151. [CrossRef]
31. Ullah, M.E.; Saeed, S.T.; Mohammed, N.A.; Idress, M.; Aslam, M.N.; Khan, I.; Oqilat, O.; Khan, M.S. Prandtl ternary nanofluid flow with MHD, porosity, and thermal effects over a 3D stretching surface with convective boundary conditions. *Int. J. Thermofluids* **2025**, *30*, 101451. [CrossRef]
32. Aslam, M.N.; Junaid, M.S.; Saeed, S.T.; Zhang, J.; Almehizia, A.A. Analysis of MHD Williamson hybrid nanofluid flow with Cattaneo–Christov heat flux over a stretching cylinder: An artificial intelligence approach. *J. Appl. Math. Mech./Z. Angew. Math. Mech.* **2025**, *105*, e70244. [CrossRef]
33. Ali, A.; Aslam, M.N.; Junaid, M.S.; Al-Zubaidi, A.; Sohail, T.; Saeed, S.T. Thermal stratification of Darcy- Forchheimer nano-fluid flow with Cattaneo-Christov heat flux over a Riga plate: A mathematical analysis. *Case Stud. Therm. Eng.* **2025**, *74*, 106794. [CrossRef]
34. Saleem, M.; Al-Zubaidi, A.; Radwan, N.; Saleem, S.; Adawi, H. Thermal effects of ternary Casson nanofluid flow over a stretching sheet: An investigation of Thomson and Troian velocity slip. *Case Stud. Therm. Eng.* **2025**, *65*, 105561. [CrossRef]
35. Kezzar, M.; Dib, A.; Ayub, A.; Tabet, I.; Sari, M.R.; Wahab, H.A.; Hussain Shah, S.Z. Duan Rach approach solution of MHD flow of ternary hybrid Casson magnetized nanofluid in converging/diverging geometry with velocity slip effects. *Numer. Heat Transf. Part A Appl.* **2025**, *86*, 8525–8542. [CrossRef]
36. Patnaik, N.; Shaw, S.; Thatoi, D.N.; Nayak, M.K. Bödewadt slip flow of Casson ternary hybrid nanofluid due to stretching rotating disk. *J. Nanofluids* **2023**, *12*, 1251–1259. [CrossRef]
37. Nath, R.S.; Deka, R.K. A numerical investigation of the MHD ternary hybrid nanofluid (Cu-Al_2O_3-TiO_2/H_2O) past a vertically stretching cylinder in a porous medium with thermal stratification. *J. Adv. Res. Fluid Mech. Therm. Sci.* **2024**, *116*, 78–96. [CrossRef]
38. Cao, W.; Animasaun, I.L.; Yook, S.-J.; Oladipupo, V.A.; Ji, X. Simulation of the dynamics of colloidal mixture of water with various nanoparticles at different levels of partial slip: Ternary-hybrid nanofluid. *Int. Commun. Heat Mass Transf.* **2022**, *135*, 106069. [CrossRef]
39. Rosca, A.V.; Rosca, N.C.; Pop, I. Slip effects on the flow and heat transfer of nanofluids over a stretching/shrinking sheet. *Int. J. Numer. Methods Heat Fluid Flow* **2020**, *30*, 2501–2521. [CrossRef]
40. Animasaun, I.L.; Ibraheem, R.O.; Mahanthesh, B.; Babatunde, H.A. A meta-analysis on the effects of haphazard motion of tiny/nano-sized particles on the dynamics and other physical properties of some fluids. *Chin. J. Phys.* **2021**, *71*, 512–528.
41. Oztop, H.F.; Abu-Nada, E. Numerical study of natural convection in partially heated rectangular enclosures filled with nanofluids. *Int. J. Heat Fluid Flow* **2008**, *29*, 1326–1336. [CrossRef]

Disclaimer/Publisher's Note: The statements, opinions and data contained in all publications are solely those of the individual author(s) and contributor(s) and not of MDPI and/or the editor(s). MDPI and/or the editor(s) disclaim responsibility for any injury to people or property resulting from any ideas, methods, instructions or products referred to in the content.